

Morphology and electrical characteristics of polymer: Fullerene films deposited by electrospray

Xin-Yan Zhao^{a,b}, Zui Tao^a, Weiwei Yang^b, Kaichen Xu^c, Lu Wang^d, Yuanyuan Jiang^e, Qianchen Zhang^a, Zhiqiang Gao^f, Baoxiu Mi^{c,*}, Minghui Hong^{c,*}, Weiwei Deng^{b,*}

^a Key Laboratory of Flexible Electronics (KLOFE) & Institute of Advanced Materials (IAM), Nanjing Tech University (Nanjing Tech), 30 South Puzhu Road, Nanjing 211800, China

^b Department of Mechanics and Aerospace Engineering, Southern University of Science and Technology, Shenzhen 518055, China

^c Department of Electrical and Computer Engineering, National University of Singapore, 4 Engineering Drive 3, 117576 Singapore, Singapore

^d Key Laboratory for Organic Electronics & Information Displays (KLOEID), Jiangsu Engineering Centre for Plate Display & Solid State Lighting, Institute of Advanced Materials (IAM), Nanjing University of Posts & Telecommunications, Nanjing 210023, China

^e Department of Mechanical Engineering, Virginia Polytechnic Institute and State University (Virginia Tech), Blacksburg, VA 24061, USA

^f Key Laboratory of Flexible Electronics & Institute of Advanced Materials, Jiangsu National Synergetic Innovation Center for Advanced Materials (SICAM), School of Material Science and Engineering, Nanjing University of Posts & Telecommunications, Nanjing 210023, China

ARTICLE INFO

Keywords:

Electrospray

Morphology

Polymer:fullerene

Electrical characteristics

Raman spectrum

ABSTRACT

Electrospray (ES) has emerged as an attractive approach to fabricate thin-film organic photovoltaic devices. However, the morphological properties and their implication to electrical characteristics of polymer:fullerene blends deposited by this method have not been clearly understood yet. In order to uncover the interplay of nanoscale morphology and electrical properties of ES-deposited films, both the residues of single droplets and thin films from the overlapping of multiple droplets were investigated by various characterization techniques. The surface morphology was demonstrated in details by the optical microscope (OM) and atom force microscope (AFM). The ordering structures and aggregation of the polymer were identified by the Raman and UV–vis spectroscopic investigations. The spatially distribution map of the P3HT aggregation states was analyzed by fitting the C¹C mode of P3HT with Lorentzian functions. The conductive atomic force microscopy (C-AFM) was used to quantify local currents and reveal the correlation between the nanostructure and charge-transport mobility. Both surface morphology and aggregation of the P3HT were found to strongly depend on the overlapping boundaries formed by the dry residues of individual droplets. More P3HT aggregation present at the boundaries. However, boundaries also show significantly higher charge-transport resistance thus lower current. Thin films deposited with less droplet evaporation exhibit more homogenous morphology, more uniform phase segregation, and consequently higher charge mobility.

1. Introduction

Organic electronic devices have attracted much attention due to low-cost and abundant organic materials as well as the potential of flexible thin-film devices fabricated by roll-to-roll processes. Recently, the power conversion efficiency (PCE) of OPVs has exceeded 12% [1–3], mainly due to the development of novel polymers with small optical band gaps. Besides the breakthrough in new active materials and interface engineering, fabrication methods that are scalable, low-cost, and compatible with roll-to-roll manufacturing play a vital role for commercialization of organic electronic devices. To that end, technologies such as inkjet printing [4,5], screen printing [6,7], slot-die coating [8,9] and pneumatic spray coating [10–12] have been

intensively investigated. Electrospray (ES), an electrohydrodynamic liquid atomizing technique, has emerged as an attractive approach to fabricate thin-film organic electronic devices such as organic light-emitting diodes (OLED) [13,14], organic thin-film transistors [15] and organic photovoltaics (OPV) [16–29]. Most recently, ES has been used to fabricate perovskite solar cells [30–32]. ES has unique advantages for organic thin films deposition for three reasons [33,34]: (i) the size of the quasi-monodispersity droplets is controllable from sub-micron range to about 100 μm; (ii) the uniform droplet size allows fine tuning of the active layer thickness and morphology; (iii) the charged droplet can be guided through electric field manipulation toward the substrate and thus result in virtually no material waste. ES-deposited organic photovoltaic devices (OPVs) achieving almost equal PCEs with spin

* Corresponding authors.

E-mail addresses: iambxmi@njupt.edu.cn (B. Mi), elehmf@nus.edu.sg (M. Hong), dengww@sustc.edu.cn (W. Deng).

coating ones have been reported by our groups and other researchers [16–19].

One of the most remarkable features of OPVs is the use of the bulk heterojunction (BHJ) active layer forming by the blend of conjugated polymers and fullerenes, where intermixed phases provide donor/acceptor interfaces for exciton dissociation. After the exciton dissociation, the positive and passive charges transport toward the anode and the cathode through purer phases of polymer and fullerene, respectively. Therefore, the morphology of the blend active layer influences both the exciton dissociation and the charge transport, thus the optimization of the morphology is essential to increase efficiency for a particular set of materials. The morphology in polymer: fullerene blends deposited by spin coating has been intensively studied, and some consensus have been reached on how the three-phase network (intermixed, pure polymer and pure fullerene) could be controlled by the processing conditions such as pre-/post- annealing and additives [35–38]. However, corresponding investigation of the polymer: fullerene blend thin-film morphology deposited by other methodologies, especially the roll-to-roll compatible methods, are still lacking.

This work aims to systematically investigate the relationships between ES processing conditions, thin film morphology and electrical characteristics. ES process the thin film is formed by piling up of ‘coffee rings’ generated from individual droplets falling on the substrate, which is fundamentally different from the spin-coated films. To achieve high-efficiency devices, clear understanding of the nanoscale morphology and phase segregation properties of the ES-deposited polymer: fullerene thin film is important. We performed detailed studies for P3HT:PCBM, which is a classic blend system that serves as a benchmark model system for the general behaviour of polymer: fullerene thin films. The insights gained from this study will be transferable to other polymer: fullerene systems. Two types of samples are prepared: (i) the individual droplet deposition that forms isolated circular residue with thicker outer rims and thinner central regions; such patterns are often referred as coffee rings; and (ii) continuous films formed by overlapping and drying of multiple droplets. We will study the nanoscale morphology of the single coffee rings and continuous films, as well as the interplay between morphology and the electrical properties by various techniques such as the optical microscope (OM), atom force microscope (AFM) and Raman spectroscopy images.

2. Experimental

2.1. Film deposition

The typical electro spray deposition apparatus is shown in Fig. 1. The ES setup consists of a syringe pump, a DC high voltage power supply, a metal nozzle, and a hot plate placed on a motorized stage. The distance between the needle tip and the substrate was kept at 5 cm. A high voltage of 2.5–4 kV was applied between the nozzle and the substrate to generate stable electro spray in the cone-jet mode [16].

Patterned indium tin oxide (ITO) coated glass substrates were cleaned by sonication in a sequence of diluted Hellmanex solution, deionized (DI) water, acetone, and isopropyl alcohol (IPA) baths for 15 min each and then dried at 80 °C for more than 1 h prior to use. After drying, the substrates were treated by plasma for 45 s. Then the Poly(3,4-ethylenedioxythiophene) (PEDOT:PSS, CLEVIOS P VP AI 4083, Heraeus) solution was spin-coated onto the clean ITO/glass substrates under 3500 rpm for 60 s and annealed at 120 °C for 15 min. The Poly(3-hexylthiophene-2,5-diyl) (P3HT, Sigma Aldrich) and Phenyl C₆₁ butyric acid methyl ester (PC₆₀BM, NanoC) with a weight ratio of 1:0.8 were dissolved in 1,2-Dichlorobenzene (DCB, Sigma Aldrich) at a concentration of 1.8 mg/ml, and the solution was stirred overnight at 45 °C in a glove box. As has been discussed in our previous work [16], to boost the electrical conductivity of the P3HT:PCBM solution, the acetic acid (Aladdin) was used as the additive (15 vol%) and the mixture was stirred for 1 h before ES. Then the solution was electro sprayed onto the PEDOT:PSS substrate. The P3HT:PCBM solution was injected through the nozzle at flow rates of 0.4, 0.7 and 1.1 ml/h and the substrate temperatures of 25, 40 and 90 °C, respectively.

For the spin coated reference samples, 20 mg P3HT and 16 mg PCBM were dissolved in 1 ml DCB, which was stirred overnight prior to use. The solution was spin coated on the PEDOT:PSS coated ITO/glass at 1000 rpm for 180 s and dried for more than 2 h in the glovebox.

2.2. Devices fabrication

The ES process was performed in air at room temperature. All samples were transferred in a thermal evaporator for metal electrode (Al of 100 nm) deposition at the pressure of 4×10^{-6} mbar. The active area of each device was 9 mm². Then the devices were post-annealed at 120 °C for 10 min in the glove box. The current density-voltage (*J-V*) characteristics were examined using a Keithley 2400 source measuring unit under simulated AM 1.5G illumination (100 mW cm⁻²) with a

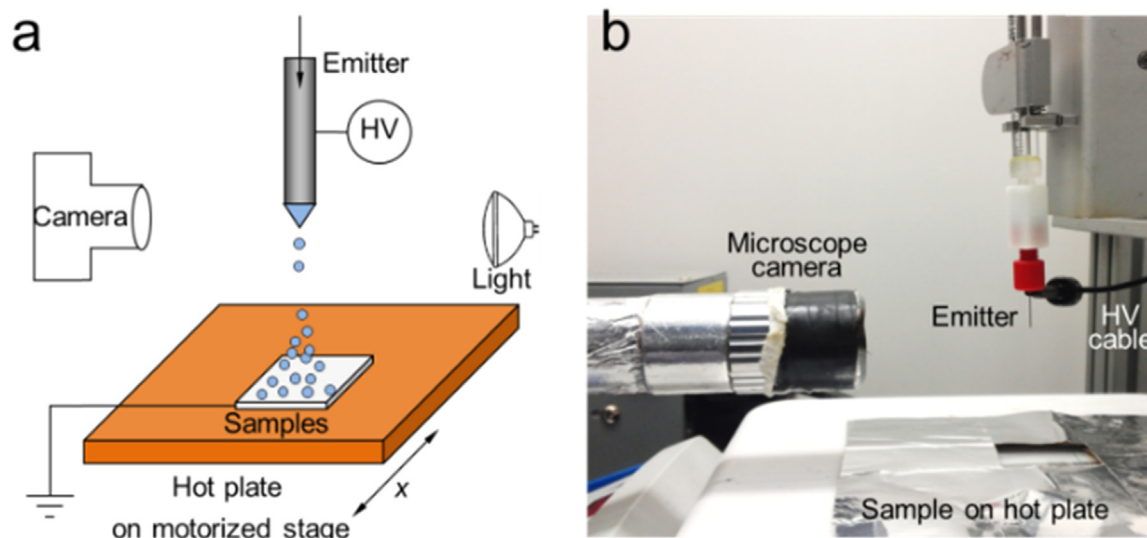


Fig. 1. (a) Schematic illustration of the electro spray setup, (b) photograph of the electro spray setup.

solar simulator. The hole-only devices were fabricated with the structure of ITO/PEDOT/P3HT:PCBM/Au.

2.3. Characterization

The optical microscopy (LV150, Nikon) and AFM (XE7, Park System Inc) were used for the surface morphological investigations. The AFM was also configured in the conducting mode to quantify local currents. The cross-section images were obtained by scanning electron microscope (SEM, Hitachi s-4800). The Confocal Raman Microscope (alpha300R, WiTec Company) was used to study the material distribution and Raman spectra of single droplet residues of continuous thin films. The absorption spectra of the active films were measured using a UV–vis Spectrometer (Lambda 35, PerkinElmer). The current density–voltage (J – V) characteristics were measured using a Keithley 2400 source measuring unit to study the mobility of hole only devices.

3. Results and discussion

3.1. Coffee ring structure of single droplet residues

As the basic units that make up the thin film, the configuration of the single droplet residues is essential to the morphology and electrical characteristics of the ES-deposited film. In order to study the morphological changes that take place at different process conditions, we prepared nine P3HT:PCBM blend films at three flow rates (0.4, 0.7 and 1.1 ml/h) combined with three substrate temperatures (25, 40 and 90 °C). To reveal the nanomorphology of the single coffee rings, the ES deposition time is only 10 s to ensure isolated droplet deposition instead of formation of continuous films.

From the OM images in Fig. 2a, we observe the variation of the circular residue size and shape for different combinations of flow rates and substrate temperatures. The diameter of the circular residues increases with the increase of flow rate or the decrease of substrate temperature. Average diameters of the circular residues in the OM images at nine process conditions are listed in Table 1. The microstructure of the single droplet residues is more clearly identified by the AFM images in Fig. 2b. The droplet residue resembles a dish with thick rim. Such residue shapes are often termed as “coffee ring”, which is caused by Marangoni effect. Confocal Raman microscopic measurements were performed to get insight into the component distribution within a single droplet residue. The Raman intensity in Fig. 2c reflects the thickness of the region being examined: high intensity (bright area) corresponds to thick area while low intensity (dark area) corresponds to thin area. The component distribution revealed by the Raman intensities is consistent with the AFM results in Fig. 2b.

Marangoni flows are driven by the thermocapillary effect from surface tension gradients [39,40]. Surface tension, γ , is an interfacial property with units of N/m. The change of γ at different locations on the surface leads to non-zero gradient $\nabla\gamma$, which is essentially a traction stress that can drive the fluid flow. $\nabla\gamma$ can arise with a temperature gradient (∇T). For a sessile droplet with contact angle less than 90°, the evaporation rate at the liquid/solid contact line is higher than the rest of the region [39], giving rise to the temperature gradient pointing from the top of the droplet toward the contact line. Such temperature gradient causes the surface tension gradient that drives the flow to the contact line. The higher evaporation rate at the contact line and continuous liquid inflow gradually accumulate the dried rim region and drains the central area to form the coffee-ring shape. Higher substrate temperatures correspond to stronger Marangoni flows that build thicker rim.

It is noteworthy that the center of the circular residues produced at low temperature appears to be not smooth with clusters of bumps, as illustrated by the enlarged view of the AFM image of S8 in Fig. 3a. Although the bumps are needle-shaped in Fig. 3a, they are not as sharp because the length scale of the thickness (z) is three orders of

magnitude finer than the substrate plane (x - y). The clusters disappear when temperature is relatively high at 90 °C. The formation of clusters can be attributed to the fluid dynamic instability during drying process as demonstrated in Fig. 3b. Such instability is also likely caused by the Marangoni effect. When a thin layer of liquid is heated from below (Fig. 3b), the external perturbation causes the local liquid layer to become thinner, i.e., the surface becomes closer to the underlying heat source. Thus, the local surface temperature will rise and the surface tension will be lower than the surrounding areas, causing flow away from the depressed region and further thinning of the liquid layer until rupture. The simultaneous rupture of multiple spots may eventually form the clusters of bumps shown in Fig. 3a.

3.2. Continuous thin films formed by droplet overlapping

Thin continuous films (~ 200 nm) were fabricated at three flow rates (0.4, 0.7 and 1.1 ml/h) combined with three substrate temperatures (25, 40 and 90 °C) to investigate the film morphology evolution according to different processing conditions. In our previous work, we proposed a model to explain the ES-deposited film morphology. This model uses the Damköhler (Da) number [17] (defined as the ratio of droplet evaporation time to residence time) to explicitly consider the collective effect from several process parameters:

$$Da = \left(\frac{8\sqrt{2}}{\varepsilon_0^{2/3}} \right) (\gamma k)^{1/6} \left(\frac{H^2}{VQ^{3/2}} \right) \left(\frac{D_{diff} \mu \rho_g}{\rho^{5/3}} \right) \left(\frac{P_v}{P_0} \right), \quad (1)$$

where γ is the liquid-air interfacial tension, k the electrical conductivity, ρ the liquid mass density, ε_0 the vacuum permittivity, H the distance between the nozzle and the ground electrode, V the applied voltage, Q the liquid flow rate, D_{diff} the mass diffusivity of the vapor molecule to the ambient environment (usually air), μ the viscosity of the ambient air, ρ_g the solvent vapor density and P_v/P_0 the ratio of vapor pressure of the solvent to ambient pressure. The Da number is used in this work to clarify the relationship between the nanoscale morphology of thin films and the ES-process condition.

The surface appearance of the thin films is illustrated by the OM images in Fig. 4a. At low temperature and high flow rate (corresponding to small Da number) the boundaries between the circular residues is ambiguous and more continuous films are formed. In the film fabricated at $T = 25$ °C and $Q = 1.1$ ml/h (with the smallest Da number among the nine conditions), the boundaries almost disappear and the film seems continuous. The status of the boundaries between circular residues and the roughness of surfaces are demonstrated by the AFM imagers in Fig. 4b. The film surface becomes smoother with the decrease of Da number. The form of the boundaries and the surface roughness of the thin films are consistent with the rim of the single droplet residue as demonstrated in Fig. 2b. The single coffee rings with thicker rims constitute more obvious boundaries and rougher surfaces in thin films.

Besides the morphology of the thin film, the continuity in the bulk of the blended thin film affect the charge-transport resistance significantly. In the spin coated films, nanostructures inside the bulk are naturally homogeneous. However, the bulk nanostructures in the ES-deposited films depend on the piling-up situation of the droplets during the ES process. SEM images (Supporting information Fig. S1) of the cross section in the samples for S3 ($Da = 1.28$), S5 ($Da = 0.10$) and S8 ($Da = 0.05$) show no cracks or holes in the active layer, which suggests that the pilling up of the droplets is rather dense to produce compact films.

The ordered structures of the polymer in the polymer: fullerene blend system have important contributions to both the charge-carrier mobility and the light absorption in the active layer [38,41]. For the spin-coated polymer: fullerene blends, many efforts have been devoted to finding the optimal functional form of the nanoscale phase domains and the intra- and intermolecular interactions in blended donor-

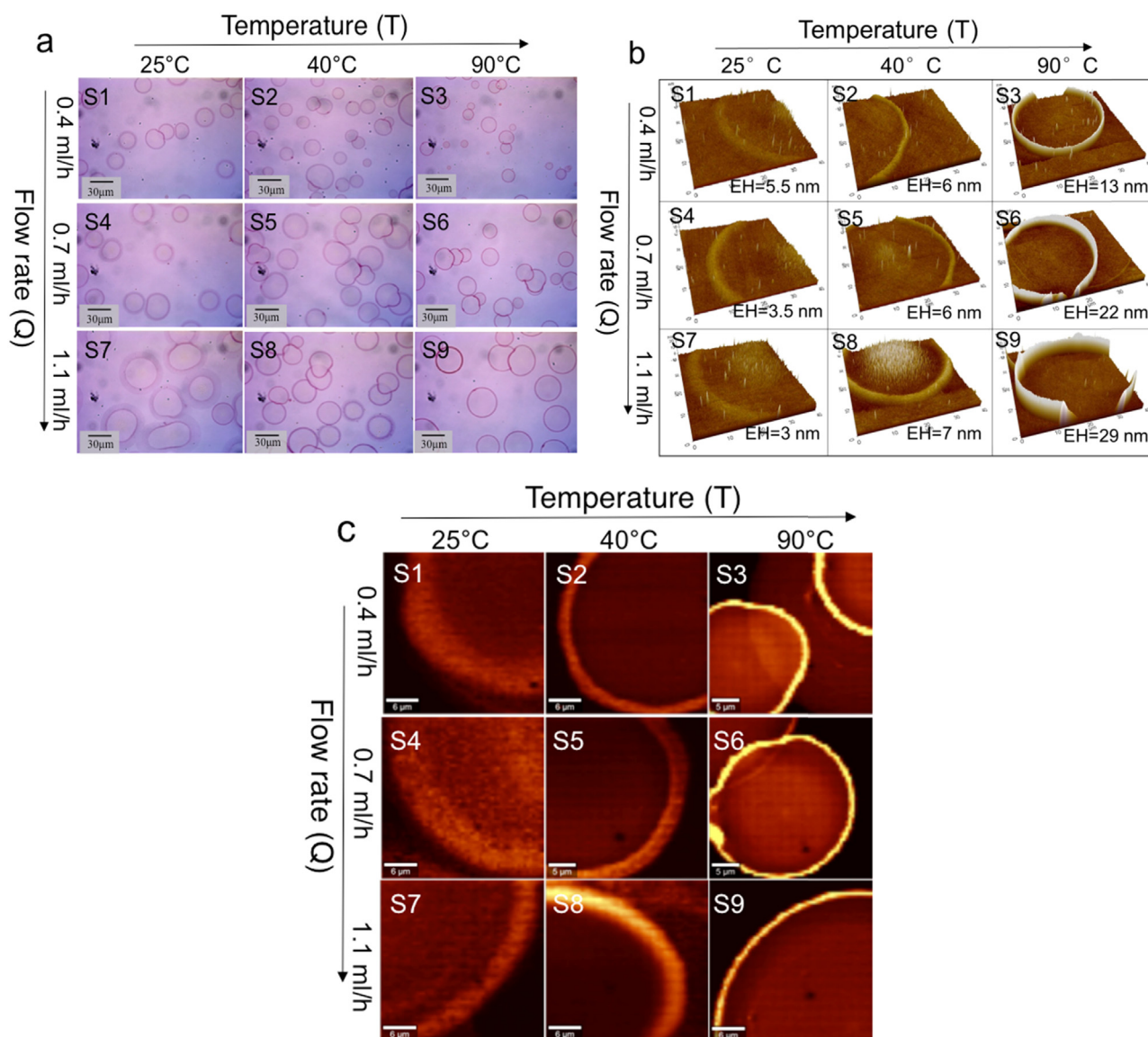


Fig. 2. (a) Optical microscope images (b) AFM images (EH: edge height, i.e., the altitude difference between the edge and the substrate) and (c) Raman intensity distribution of coffee rings produced at different flow rates and substrate temperatures during ES process.

acceptor thin films [42,43]. Here we used the resonance Raman imaging to gain insights to the morphological heterogeneity on the aggregated and unaggregated P3HT chains in ES-deposited P3HT/PCBM films. Raman spectra were obtained by exciting P3HT/PCBM materials using a 488 nm laser.

The Raman intensity map in Fig. 5a shows the intensity distribution of materials in the continuous thin films. ES processed film with smaller Da number produces more continuous films, which is consistent with the OM (Fig. 4a) and AFM (Fig. 4b) images, in which samples with smaller Da number exhibit ambiguous and thinner boundaries. Raman spectra of typical residue areas in Sample S5 are shown in Fig. 5b. The Raman spectra exhibit two vibrational modes: C=C symmetric stretch

(around 1450 cm^{-1}) and C-C stretch (around 1380 cm^{-1}) modes in the thiophene ring. The two main in-plane ring skeleton modes are sensitive to conjugation length of P3HT molecules [35,44–46]. The change in the P3HT C=C symmetric stretch mode can be attributed to ordered P3HT (centered near 1450 cm^{-1}) and disordered P3HT (centered near 1470 cm^{-1}) [35,44–46]. The shift in C=C peak position toward higher frequency suggests less order of P3HT. The C=C mode can be fitted with two Lorentzian functions (see Fig. 5b), revealing the relative contributions of both aggregated ($I_{\text{C-C}}^{\text{agg}}$, red dashed curve) and unaggregated ($I_{\text{C-C}}^{\text{un}}$, green dot-dashed curve) components [46,47]. The $I_{\text{C-C}}^{\text{agg}}$ component represents P3HT chains with higher intra- and interchain order and with longer conjugation lengths. The $I_{\text{C-C}}^{\text{un}}$

Table 1

The process conditions (flow rate and temperature), Da numbers and average diameters of the individual circular residues in the OM images of the nine samples.

Samples	S1	S2	S3	S4	S5	S6	S7	S8	S9
Flow rate (ml/h)	0.4	0.4	0.4	0.7	0.7	0.7	1.1	1.1	1.1
Temperature (°C)	25	40	90	25	40	90	25	40	90
Da number	0.13	0.246	1.279	0.056	0.102	0.553	0.028	0.052	0.281
Average diameter (μm)	21	19	17	26	25	23	36	28	29

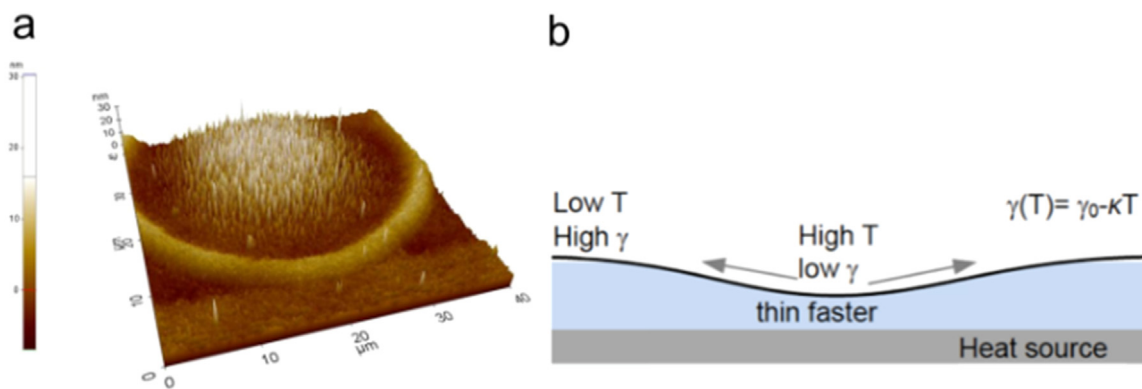


Fig. 3. Marangoni effect: (a) enlarged view of the AFM image of sample S8, (b) Flow instability driven by surface tension gradient.

component corresponds to chains with lower intra- and interchain order, i.e., unaggregated P3HT chains and shorter conjugation lengths. Therefore, the ratio of ordered P3HT phase in P3HT/PCBM blend films can be estimated from the ratio of Raman intensities of the two components: $R = I_{C-C}^{agg}/I_{C-C}^{un}$ [46,47]. Higher R values suggest a greater number of I_{C-C}^{agg} species due to increased phase segregation. The R maps (Fig. 5c) clearly show the spatially morphology-dependent variations in the ratio of aggregated and unaggregated P3HT components in the P3HT:PCBM blend thin films. In each sample, R values are higher at the boundary areas. For example, in the R map of S5, the red circle represents a region of high R value ($R = 3.58$), and purple triangle represents a region of low R value ($R = 1.31$). This indicates that the boundary areas contain more aggregated P3HT components than the center of the coffee rings. Comparison of R images of different samples suggest averaged R value generally increases with smaller Da number, revealing more cofacial π - π stacked structures are formed at ES process with lower temperatures and higher flow rates. On the other hand, the morphology of samples with smaller Da numbers are more homogeneous, as revealed by the AFM images (Fig. 4b) and Raman intensity images (Fig. 5a). Correspondingly, the R values of these samples are more evenly distributed, suggesting uniform phase segregation.

The contributions of aggregated and unaggregated components can also be investigated by the UV–vis absorption spectroscopy, which indicates the average heterogeneity morphology characteristics over the entire P3HT:PCBM blend thin films. As seen in Fig. 5d, most noticeable is a red shift in the electro spray sample compared to the spin-cast sample, and similar results were reported in our previous works

[16,17]. The red shift indicates more ordered crystalline involves an enhanced conjugation length hence a shift of the absorption spectrum to lower energies. For the ES-deposited thin films, samples produced at the lowest substrate temperature, 25 °C (corresponding to smaller Da numbers), show higher intensity and more distinguished shoulders at 0–1 peak (~ 560 nm) and 0–0 peak (~ 600 nm), indicating the increased interchain interaction among the P3HT chains. With the substrate temperature raised to 40 °C, and the shoulders at ~ 560 nm and ~ 600 nm decline slightly. When the substrate temperature was raised to 90 °C (corresponding to the largest Da numbers) the shoulders decline significantly, indicating the reduction of effective conjugation length and increase in disorder in P3HT packing. The overall morphology-dependent variations of the P3HT:PCBM blend layers revealed by the UV–vis absorption spectra is consistent with those presented by the R images.

3.3. Electrical properties of the ES-deposited thin films

Understanding the correlations between the morphological nanostructure and the photocurrent generation is desirable for seeking approaches to improve device performance. To map the spatial morphology-dependent polymer aggregation state to the local electrical properties in the P3HT/PCBM blend photovoltaic device, the conductive atomic force microscopy (C-AFM) was used to simultaneously characterize the local current density and surface topography. In C-AFM, a platinum (Pt) coated cantilever tip forms a local electrical contact and the substrate forms another electrical contact where a bias

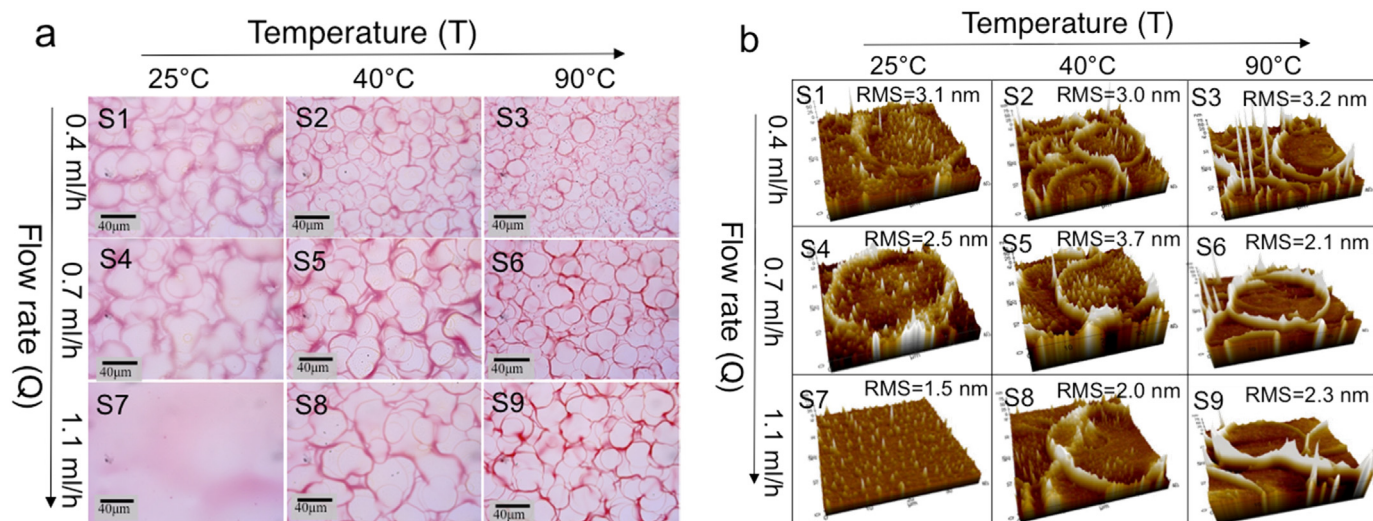


Fig. 4. Surface morphology of continuous thin films produced at different flow rates and substrate temperatures by ES process: (a) optical microscopy images, (b) AFM images.

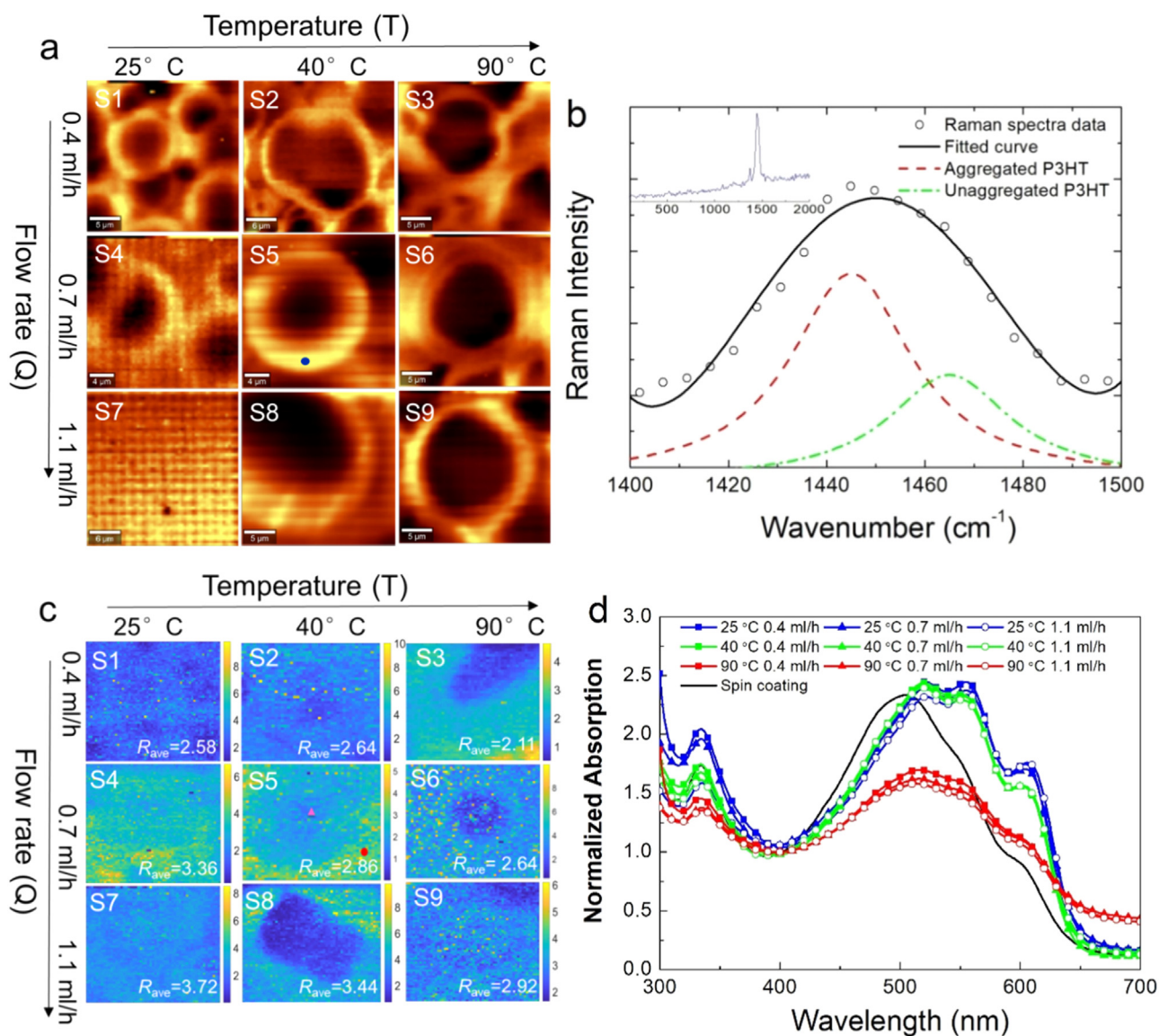


Fig. 5. (a) Raman intensity distribution, (b) Raman spectrum of the blue dot in sample S5 (inset shows the complete spectrum), fitted with two Lorentzian functions (dashed traces) of the form $y_1 + A_1\{\Gamma_2/[(x-x_1)^2 + \Gamma_2]\} + y_2 + A_2\{\Gamma_2/[(x-x_2)^2 + \Gamma_2]\}$, showing the relative contributions of aggregated and unaggregated P3HT components, (c) Ratio images of Lorentzian components (R) derived from the Raman spectra, where R_{ave} is the average value of R, and (d) UV-vis spectra of continuous thin films produced at different flow rates and substrate temperatures by ES process.

voltage is applied. Combining the local current density profile with the surface topography, correlation of local morphological characteristics and electrical properties can be inferred.

Fig. 6a illustrates the C-AFM current maps of thin films (surface topography and current map of the single coffee ring see Supporting information Fig. S2). In our C-AFM measurements, holes are the major injected carriers. Therefore, the hole current images were obtained to examine conductivity variations and map the P3HT conducting network in the P3HT:PCBM blends. Fig. 6a clearly shows the high (bright region) and low (dark region) current corresponding to the local morphology. In the hole current map of each samples, the current is higher at the flat central areas of the coffee rings while the boundary areas show lower current. However, R values (Fig. 5c) are higher at boundary areas, suggesting higher aggregation of P3HT, which is considered to be beneficial to hole transport. Therefore, the lower hole current at the boundary areas could not be explained by the aggregation of P3HT but might be attributed to two accounts: the ununiform thickness and the charge carrier blocking caused by overlapping boundaries. The rim is significantly thicker than the center, especially for the samples with

larger Da number, therefore may have larger resistance at the rim. To eliminate the influence of the thickness variation, the current density map is normalized by the surface topography map (Supporting information Fig. S3). The normalized current maps (Fig. 6b) demonstrate similar patterns with the C-AFM current maps that the current is lower at boundary areas. This suggests that the lower current at boundary areas should not be mainly attributed to the influence of the non-uniformity of film thickness but to the charge carrier blocking caused by overlapping boundaries. Previous literature has demonstrated that the interfacial boundaries between the coffee rings caused high charge-transport resistance [19].

Comparison of the current density maps of thin films deposited at different process conditions shows that the hole current generally increase with decreasing Da number, and the sample S7 (with the lowest Da number) has the highest average hole current. This can be explained by both the surface roughness and the aggregation of polymer. Samples with lower Da numbers have smoother surface and ambiguous boundaries, which reduces the charge-transport resistance induced by the boundaries. Meanwhile, samples with lower Da numbers have higher

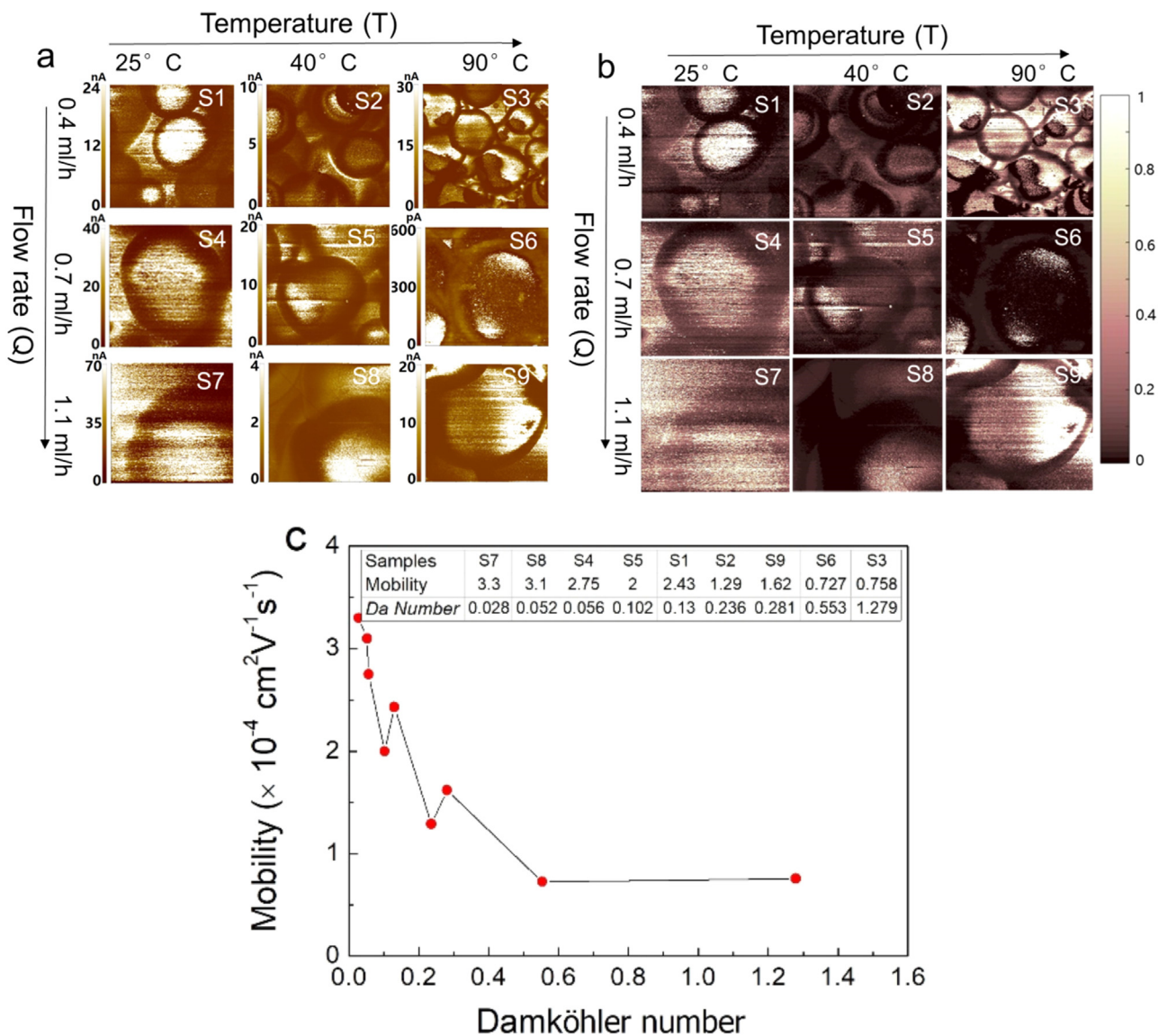


Fig. 6. Electrical properties of the ES-deposited thin films: (a) current density maps characterized by C-AFM; (b) the normalized current density maps; (c) carrier mobility vs. Damköhler numbers.

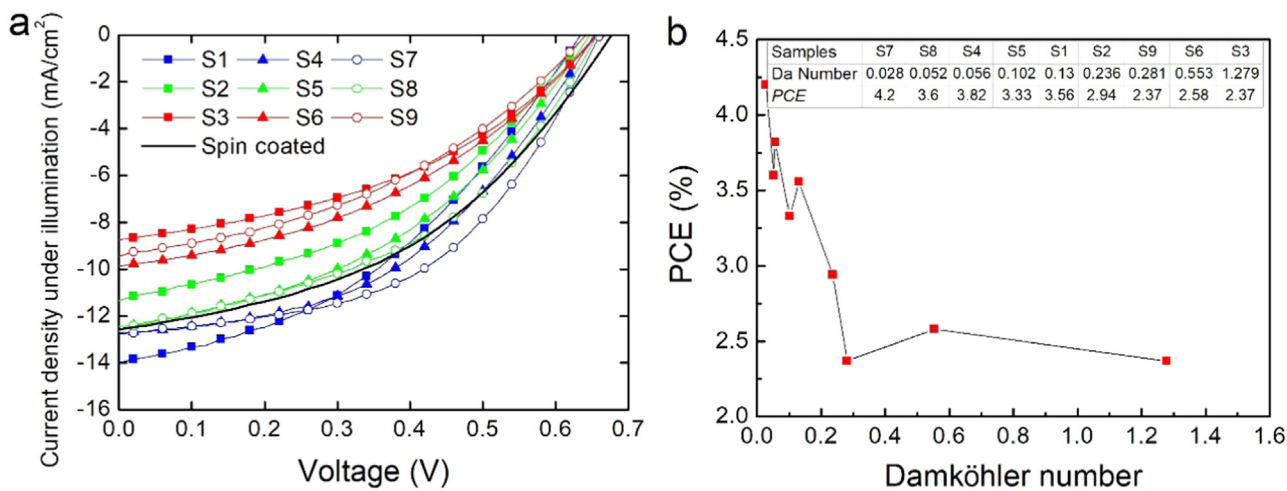


Fig. 7. (a) J-V curves of OPV devices under AM 1.5G illumination at 100 mW/cm². (b) PCEs for OPV devices with ES-coated P3HT:PCBM layers deposited with different Da numbers.

Table 2
Performance parameters of OPV devices.

Samples	J_{sc} [mA cm ⁻²]	V_{oc} [V]	FF [%]	PCE [%]
S1	14.00	0.63	40.33	3.56
S2	11.35	0.64	40.48	2.94
S3	8.73	0.65	41.67	2.37
S4	12.72	0.65	46.17	3.82
S5	12.43	0.65	41.18	3.33
S6	9.87	0.65	40.20	2.58
S7	12.75	0.66	49.95	4.20
S8	12.64	0.65	43.84	3.60
S9	9.46	0.64	39.09	2.37
Spin coated	12.61	0.67	43.11	3.64

averaged R , i.e., more aggregated P3HT components, which favors the hole transport. The hole mobilities were measured by hole-only devices using a space-charge-limited-current model (see Supporting information). Fig. 6c illustrated the correlation between hole mobilities and the Da number, and the inset lists the data. The hole mobility increases with the decrease of Da number, which is consistent with the regularity represented by the R images and current density maps. In our earlier work [17], we demonstrated the influence of Da number on performance of devices based on ES-deposited P3HT:PCBM active layers, showing that the power conversion efficiency (PCE) of devices monotonically increased with the decrease of Da number. This trend is consistent with the mobility variation with Da number illustrated in Fig. 6c. We also fabricated devices using the nine process conditions discussed above and referenced devices by spin coating. The current–voltage characteristics of the ES-fabricate devices as well as the referenced spin-coated device under AM 1.5G illumination are plotted in Fig. 7a, and the overall photovoltaic performances of these devices are represented in Table 2. The PCEs of the devices showed the similar monotonically trend with the variation of Da number (see Fig. 7b), i.e., the PCE increased with the decrease of Da number.

4. Conclusions

We performed detailed investigation of the morphology and the relationship between morphology and electrical characteristics of polymer: fullerene blends deposited by electrospray. Firstly, the morphology of the single droplet residues was investigated. The variation of the shape of the rim and center areas of single coffee rings with different processing conditions such as temperatures and flow rates are demonstrated. Secondly, the nanoscale morphology of ES-deposited thin films, especially the ordering structures and aggregation of the polymer were identified by analysing the Raman spectra and fitting the C=C mode in P3HT with Lorentzian functions to obtain the spatial map of the R values. Both surface morphology and aggregation of the P3HT were found to be determined by the boundaries between overlapping residues of isolated droplets. The boundary areas result in rougher surface and contain higher P3HT aggregation compared with the flat areas. Samples, produced at lower Da numbers have more homogenous morphology with ambiguous boundaries and smooth surface, as well as more uniform phase segregation and higher R value. Finally, the local current characterized using C-AFM was compared with the special morphology-dependent polymer aggregation state to reveal the correlation between the morphological nanostructure with the current generation and charge-transport mobility. By eliminating the influence of film thickness, it was found that the hole current is lower at boundary areas, and this might be attributed to the high charge-transport resistance caused by the boundaries formed by overlapping of residues of dried droplets. The hole mobilities measured using the space-charge-limited-current model illustrated that the hole mobility increases with the decrease of Da number. Therefore, process conditions with lower Da numbers are beneficial to produce polymer:fullerene blended films with

homogenous morphology, higher aggregated polymer ratio and higher charge mobility.

This work developed a detailed understanding of the relationship between processing condition, shapes of single droplet residues, thin film morphology, and electrical properties of the ES-deposited thin films. The methods and conclusions may be transferable to other polymer: fullerene material systems.

Acknowledgements

This work was financially supported by the National Natural Science Foundation of China (Nos. 61605076, 61474064), Jiangsu Government Scholarship for Overseas Studies, A*ATAR, SERC 2014 Public Sector Research Funding (PSF) Grant (SERC Project No. 1421200080). W Deng thanks the National Science Foundation (Grants No. CMMI 1301099 and CMMI 1454406) for financial support. We would like to thank Dr. Yongqian Gao for the discussion about the Lorentzian fitting of the Raman spectra.

Appendix A. Supporting information

Supplementary data associated with this article can be found in the online version at <http://dx.doi.org/10.1016/j.solmat.2018.04.013>.

References

- [1] F.C.S.P. Thanks, Heliatek sets new OPV world record efficiency of 13.2% <<http://www.heliatek.com/en/press/press-releases/details/heliatek-sets-new-organic-photovoltaic-world-record-efficiency-of-13-2>>, 2016.
- [2] W. Zhao, S. Li, H. Yao, S. Zhang, Y. Zhang, B. Yang, J. Hou, Molecular optimization enables over 13% efficiency in organic solar cells, *J. Am. Chem. Soc.* 139 (2017) 7148–7151.
- [3] F. Zhao, S. Dai, Y. Wu, Q. Zhang, J. Wang, L. Jiang, Q. Ling, Z. Wei, W. Ma, W. You, C. Wang, X. Zhan, Single-junction binary-blend nonfullerene polymer solar cells with 12.1% efficiency, *Adv. Mater.* 29 (2017) 1700144.
- [4] X. Peng, J. Yuan, S. Shen, M. Gao, A.S.R. Chesman, H. Yin, J. Cheng, Q. Zhang, D. Angmo, Perovskite and organic solar cells fabricated by inkjet printing: progress and prospects, *Adv. Funct. Mater.* 27 (2017) 1703704.
- [5] A. Teichler, J. Perelaer, U.S. Schubert, Inkjet printing of organic electronics – comparison of deposition techniques and state-of-the-art developments, *J. Mater. Chem. C* 1 (2013) 1910–1925.
- [6] X. Cao, H. Chen, X. Gu, B. Liu, W. Wang, Y. Cao, F. Wu, C. Zhu, Screen printing as a scalable and low-cost approach for rigid and flexible thin-film transistors using separated carbon nanotubes, *ACS Nano* 8 (2014) 12769–12776.
- [7] J.B. Preinfalk, T. Eiselt, T. Wehler, V. Rohner, T. Hanemann, G. Gomard, U. Lemmer, Large-area screen-printed internal extraction layers for organic light-emitting diodes, *ACS Photonics* 4 (2017) 928–933.
- [8] F. Liu, S. Ferdous, E. Schaible, A. Hexemer, M. Church, X. Ding, C. Wang, T.P. Russell, Fast printing and in situ morphology observation of organic photovoltaics using slot-die coating, *Adv. Mater.* 27 (2015) 886–891.
- [9] D. Vak, K. Hwang, A. Faulks, Y. Jung, N. Clark, D. Kim, G.J. Wilson, S.E. Watkins, 3D printer based slot-die coater as a lab-to-fab translation tool for solution-processed solar cells, *Adv. Energy Mater.* 5 (2015).
- [10] S. Arumugam, Y. Li, S. Senthilarasu, R. Torah, A.L. Kanibolotsky, A.R. Inigo, P.J. Skabara, S.P. Beeby, Fully spray-coated organic solar cells on woven polyester cotton fabrics for wearable energy harvesting applications, *J. Mater. Chem. A* 4 (2016) 5561–5568.
- [11] D. Vak, J. van Embden, W.W.H. Wong, S. Watkins, Optically monitored spray coating system for the controlled deposition of the photoactive layer in organic solar cells, *Appl. Phys. Lett.* 106 (2015).
- [12] S. Das, B. Yang, G. Gu, P.C. Joshi, I.N. Ivanov, C.M. Rouleau, T. Aytug, D.B. Geohegan, K. Xiao, High-performance flexible perovskite solar cells by using a combination of ultrasonic spray-coating and low thermal budget photonic curing, *ACS Photonics* 2 (2015) 680–686.
- [13] S. Lee, H. Koo, S. Cho, Mask-less patterning of organic light emitting diodes using electrospray and selective biasing on pixel electrodes, *Appl. Phys. Lett.* 106 (2015).
- [14] W. Hwang, G. Xin, M. Cho, S.M. Cho, H. Chae, Electrospray deposition of polymer thin films for organic light-emitting diodes, *Nanoscale Res. Lett.* 7 (2012).
- [15] C. Pitsalidis, A.M. Pappa, S. Hunter, A. Laskarakis, T. Kaimakamis, M.M. Payne, J.E. Anthony, T.D. Anthopoulos, S. Logothetidis, High mobility transistors based on electrospray-printed small-molecule/polymer semiconducting blends, *J. Mater. Chem. C* 4 (2016) 3499–3507.
- [16] X. Zhao, X. Wang, S.L. Lim, D. Qi, R. Wang, Z. Gao, B. Mi, Z. Chen, W. Huang, W. Deng, Enhancement of the performance of organic solar cells by electrospray deposition with optimal solvent system, *Sol. Energy Mater. Sol. Cells* 121 (2014) 119–125.
- [17] X. Zhao, W. Yang, C. Li, X. Wang, S.L. Lim, D. Qi, R. Wang, Z. Gao, B. Mi, Z. Chen, W. Huang, W. Deng, Effects of Damköhler number of evaporation on the

- morphology of active layer and the performance of organic heterojunction solar cells fabricated by electrospray method, *Sol. Energy Mater. Sol. Cells* 134 (2015) 140–147.
- [18] T. Fukuda, K. Suzuki, N. Yoshimoto, Y. Liao, Controlled donor-accepter ratio for application of organic photovoltaic cells by alternative intermittent electrospray co-deposition, *Org. Electron.* 33 (2016) 32–39.
- [19] J. Kim, W. Chung, K. Kim, D.Y. Kim, K. Paeng, S.M. Jo, S. Jang, Performance optimization of polymer solar cells using electrostatically sprayed photoactive layers, *Adv. Funct. Mater.* 20 (2010) 3538–3546.
- [20] S. Park, S. Kim, K. Kim, H. Joe, B. Jung, E. Kim, W. Kim, B. Min, J. Hwang, Fabrication of ordered bulk heterojunction organic photovoltaic cells using nanopatterning and electrohydrodynamic spray deposition methods, *Nanoscale* 4 (2012) 7773–7779.
- [21] M. Ali, M. Abbas, S.K. Shah, R. Tuerhong, A. Generosi, B. Paci, L. Hirsch, R. Gunnella, Realization of solution processed multi-layer bulk heterojunction organic solar cells by electro-spray deposition, *Org. Electron.* 13 (2012) 2130–2137.
- [22] T. Fukuda, K. Takagi, T. Asano, Z. Honda, N. Kamata, K. Ueno, H. Shirai, J. Ju, Y. Yamagata, Y. Tajima, Bulk heterojunction organic photovoltaic cell fabricated by the electrospray deposition method using mixed organic solvent, *Phys. Status Solidi-R* 5 (2011) 229–231.
- [23] Y. Kim, G. Kim, J. Lee, K. Lee, Morphology controlled bulk-heterojunction layers of fully electro-spray coated organic solar cells, *Sol. Energy Mater. Sol. Cells* 105 (2012) 272–279.
- [24] S. Park, J. Hwang, K. Kim, B. Jung, W. Kim, J. Hwang, Spray deposition of electrohydrodynamically atomized polymer mixture for active layer fabrication in organic photovoltaics, *Sol. Energy Mater. Sol. Cells* 95 (2011) 352–356.
- [25] T. Fukuda, A. Toda, K. Takahira, K. Suzuki, Y. Liao, M. Hirahara, M. Saito, I. Osaka, Molecular ordering of spin-coated and electrosprayed P3HT:PCBM thin films and their applications to photovoltaic cell, *Thin Solid Films* 612 (2016) 373–380.
- [26] T. Fukuda, A. Toda, K. Takahira, D. Kuzuhara, N. Yoshimoto, Improved performance of organic photovoltaic cells with PTB7-Th:PC 71 BM by optimized solvent evaporation time in electrospray deposition, *Org. Electron.* 48 (2017) 96–105.
- [27] S.K. Shah, R. Gunnella, L. Hirsch, M. Abbas, Stability enhancement of polymer solar cells in trilayer configuration, *Thin Solid Films* 640 (2017) 104–108.
- [28] K.K. Khanum, J.A. Krishnaswamy, P.C. Ramamurthy, Design and fabrication of photonic structured organic solar cells by electrospraying, *J. Phys. Chem. C* 121 (2017) 8531–8540.
- [29] A. Kimoto, H. Takaku, H. Hayakawa, M. Koseki, R. Ishihama, T. Aoyama, Y. Tajima, Multilayer organic photovoltaic devices fabricated by electrospray deposition technique and the role of the interlayer, *Thin Solid Films* 636 (2017) 302–306.
- [30] S.C. Hong, G. Lee, K. Ha, J. Yoon, N. Ahn, W. Cho, M. Park, M. Choi, Precise morphology control and continuous fabrication of perovskite solar cells using droplet-controllable electrospray coating system, *ACS Appl. Mater. Interfaces* 9 (2017) 7879–7884.
- [31] S. Kavadiya, D.M. Niedzwiedzki, S. Huang, P. Biswas, Electrospray-assisted fabrication of moisture-resistant and highly stable perovskite solar cells at ambient conditions, *Adv. Energy Mater.* 7 (2017).
- [32] P. Lin, Y. Chen, T. Guo, Y. Fu, L. Lai, C. Lee, Electrospray technique in fabricating perovskite-based hybrid solar cells under ambient conditions, *RSC Adv.* 7 (2017) 10985–10991.
- [33] X. Zhao, B. Lojewski, W. Yang, T. Zhu, B. Mi, Z. Gao, W. Huang, W. Deng, Electrospray as a fabrication tool in organic photovoltaics, *Rev. Nanosci. Nanotechnol.* 1 (2012) 172–186.
- [34] A. Gomez, W. Deng, Fundamentals of cone-jet electrospray, the aerosol measurement: principles, *Tech. Appl.* (2011) 435–448.
- [35] J. Razzell-Hollis, S. Limbu, J. Kim, Spectroscopic investigations of three-phase morphology evolution in polymer: fullerene solar cell blends, *J. Phys. Chem. C* 120 (2016) 10806–10814.
- [36] Y. Liu, J. Zhao, Z. Li, C. Mu, W. Ma, H. Hu, K. Jiang, H. Lin, H. Ade, H. Yan, Aggregation and morphology control enables multiple cases of high-efficiency polymer solar cells, *Nat. Commun.* 5 (2014).
- [37] J.T. Rogers, K. Schmidt, M.F. Toney, E.J. Kramer, G.C. Bazan, Structural order in bulk heterojunction films prepared with solvent additives, *Adv. Mater.* 23 (2011) 2284.
- [38] G. Li, V. Shrotriya, J.S. Huang, Y. Yao, T. Moriarty, K. Emery, Y. Yang, High-efficiency solution processable polymer photovoltaic cells by self-organization of polymer blends, *Nat. Mater.* 4 (2005) 864–868.
- [39] L.E. Scriven, C.V. Sterlino, The Marangoni effects, *Nature* 187 (1960) 186.
- [40] H. Hu, R.G. Larson, Marangoni effect reverses coffee-ring depositions, *J. Phys. Chem. B* 110 (2006) 7090–7094.
- [41] J.A. Bartelt, Z.M. Beiley, E.T. Hoke, W.R. Mateker, J.D. Douglas, B.A. Collins, J.R. Tumbleston, K.R. Graham, A. Amassian, H. Ade, J.M.J. Frechet, M.F. Toney, M.D. McGehee, The importance of fullerene percolation in the mixed regions of polymer-fullerene bulk heterojunction solar cells, *Adv. Energy Mater.* 3 (2013) 364–374.
- [42] B. Jung, K. Kim, J. Kim, S. Kim, E. Kim, W. Kim, Inter-diffused ordered bulk heterojunction organic photovoltaics: optimized morphology for efficient exciton dissociation and charge transport, *Sol. Energy Mater. Sol. Cells* 120 (2014) 675–684.
- [43] C. Poelking, M. Tietze, C. Elschner, S. Olthof, D. Hertel, B. Baumeier, F. Wuerthner, K. Meerholz, K. Leo, D. Andrienko, Impact of mesoscale order on open-circuit voltage in organic solar cells, *Nat. Mater.* 14 (2015) 434–439.
- [44] E. Klimov, W. Li, X. Yang, G.G. Hoffmann, J. Loos, Scanning near-field and confocal Raman microscopic investigation of P3HT-PCBM systems for solar cell applications, *Macromolecules* 39 (2006) 4493–4496.
- [45] P. Veerender, V. Saxena, A.K. Chauhan, S.P. Koiry, P. Jha, A. Gusain, S. Choudhury, D.K. Aswal, S.K. Gupta, Probing the annealing induced molecular ordering in bulk heterojunction polymer solar cells using in-situ Raman spectroscopy, *Sol. Energy Mater. Sol. Cells* 120 (2014) 526–535.
- [46] Y. Gao, J.K. Grey, Resonance chemical imaging of polythiophene/fullerene photovoltaic thin films: mapping morphology-dependent aggregated and unaggregated C¹³C species, *J. Am. Chem. Soc.* 131 (2009) 9654–9662.
- [47] W.C. Tsoi, D.T. James, J.S. Kim, P.G. Nicholson, C.E. Murphy, D.D.C. Bradley, J. Nelson, J. Kim, The nature of in-plane skeleton Raman modes of P3HT and their correlation to the degree of molecular order in P3HT:PCBM blend thin films, *J. Am. Chem. Soc.* 133 (2011) 9834–9843.